Chapter 6

Creep Behavior

This chapter deals with the detailed creep behavior of the squeeze-cast Mg-5.0Al-2.0Ca-0.3Mn (wt.%) (AXM520) alloy and NCs. The creep behavior of the AXM520 alloy and NCs has been examined using impression creep tests. The observed creep rates are correlated with the as-cast microstructures of the alloy and nanocomposites. The governing creep mechanisms have been determined in the alloy and nanocomposites in the temperature and stress ranges employed. Further, the post-creep microstructural analyses of the alloy and nanocomposites have been carried out. A summary of the impression creep behavior of the AXM520 alloy and nanocomposites is presented at the end of this chapter.

6.1 Creep behavior

6.1.1 Nature of creep curves and comparison of creep responses

The creep performance of the AXM520 alloy and nanocomposites was investigated utilizing the impression creep technique. The variation of impression (indentation) depth with time at 498 K and 435 MPa for all the materials has been presented in Figure 6.1(a) over the same time duration. At the beginning of each creep curve, there is a certain jump in the indentation depth, and it is termed as the impression depth, similar to the instantaneous strain observed in a conventional tensile or compressive creep curve. The primary creep and thereafter a secondary or steady-state creep stage follow the instantaneous impression depth. A typical tensile creep curve exhibits three stages of creep, i.e., primary, secondary, and tertiary stages. However, the tertiary stage is not observed in an impression creep as the indentation took place under compressive stress. The compressive stress generally aids in forming a stable deformed zone beneath the indenter and prolongs the secondary stage. The impression velocities (dh/dt) derived for these curves are plotted in Figure 6.1(b) against time. The impression velocity initially decreased with time, then became almost constant, indicating a steady-state achieved. The decrease in impression velocity in the primary stage was attributed to the strain-hardening rate that dominated the recovery rate in the materials. After that, the strain-hardening rate and recovery rate counterbalanced each other, resulting in a steady-state creep. The creep

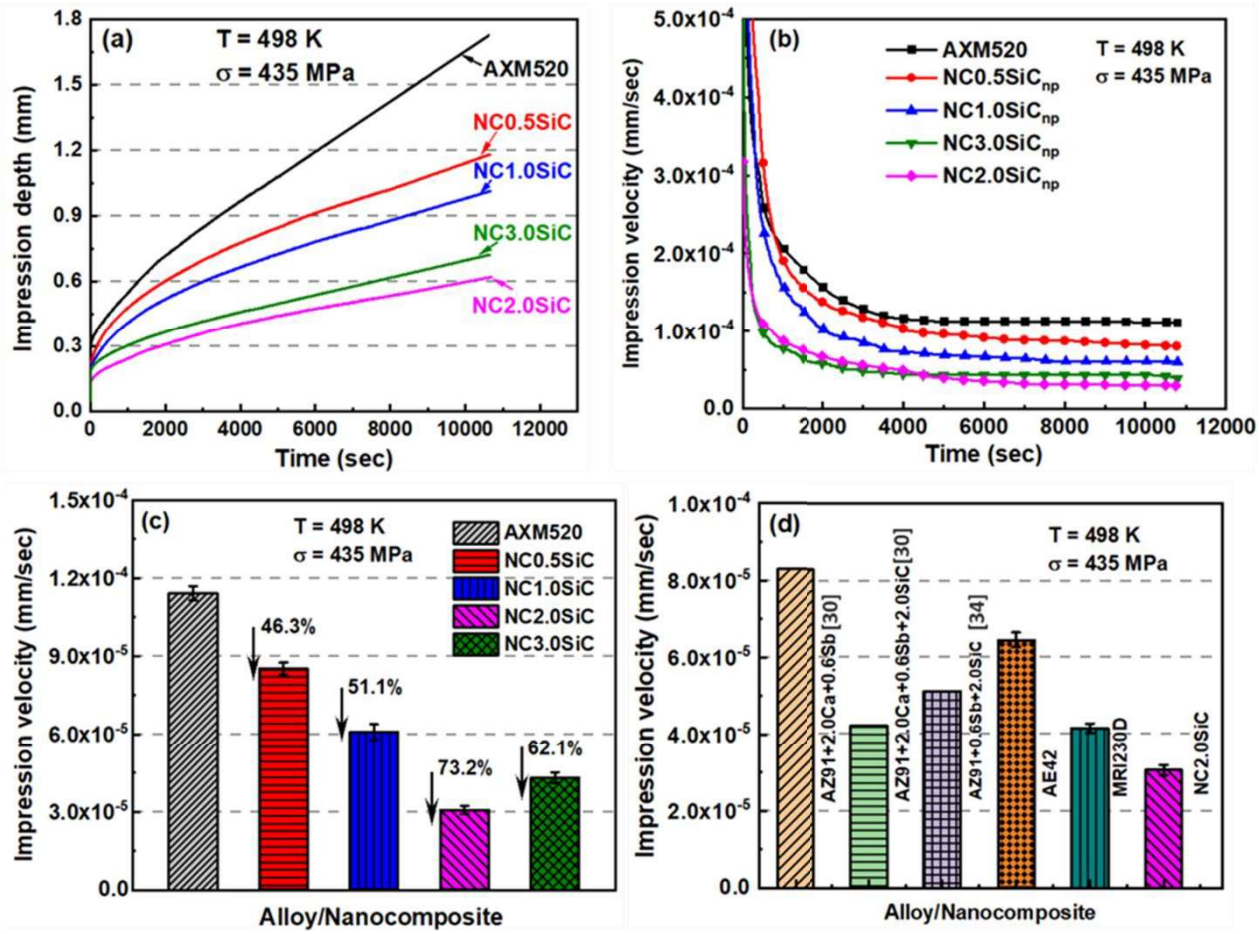

Figure 6.1 (a) Impression depth vs. time plots for the AXM520 alloy and nanocomposites nanocomposite creep tested at 498 K and 435 MPa; (b) impression velocity vs. time plots based on 'a'; and (c) steady-state impression velocities estimated from 'a'; and (d) steady-state impression velocities estimated from 'a', as well as previously reported nanocomposites, and alloy [30,34].

performance of the alloy and nanocomposites can be quantified in terms of indentation depth and steady-state impression velocity. At particular stress and temperature, a lower value of impression depth for a fixed duration or a lower value of steady-state impression velocity specifies superior creep performance. The impression depths recorded for the nanocomposites significantly reduced over the AXM520 alloy. The indentation depth gradually decreases as the SiC nanoparticles contents increase in the nanocomposites up to 2.0 (wt.%) SiC_{np}, and thus, it was the lowest in the case of NC2.0SiC. However, the impression depth did not decrease, although the fraction of SiC_{np} was changed from 2.0 to 3.0 (wt.%). The values of the V_{imp} of AXM520 and NCs are summarized in Figure 6.1(c). The impression velocities of the NCs were lower than AXM520 alloy, indicating superior creep resistance of the former materials compared to the latter. The creep performance of the NCs increased as SiC_{np} content increased; thus, the creep resistance of NC2.0SiC increased by 73.2%. However, with the further increase in the nanoparticles content, the creep resistance deteriorated, and accordingly, the NC3.0SiC exhibited a 62.1% improvement compared to the alloy. The deterioration of creep resistance of NC3.0SiC was attributed to the agglomeration of nanoparticles, resulting from the higher content of SiC_{np} in the NCs. Thornby et al. [115] explored the creep response of the Mg-(0-0.75 vol.%) CNT nanocomposites. They, too, observed that the creep performance of the NCs improved up to 0.5 vol.% CNT content, and beyond that, the creep resistance deteriorated. Further, the well-known creep-resistant AE42 and MRI230D alloys at the comparable stress and temperature (i.e., 435 MPa and 498 K) were subjected to impression creep tests, and the creep rates of these two alloys are compared with that obtained in NC2.0SiC in in Figure 6.1(d). The reported values of the AZ91+2.0Ca+0.6Sb, AZ91+2.0Ca+0.6Sb+2.0SiC, and AZ91+0.6Sb+2.0SiC are also compared with that of NC2.0SiC in Figure 6.1(d) [30,34]. Interestingly, the impression velocity of the NC2.0SiC is the lowest. Thus, it revealed the best creep performance among the standard creep-resistant alloys and nanocomposites employed for comparison.

6.1.2 Assessment of creep mechanism

A conventional tensile or compressive creep test is generally conducted at a constant temperature and constant stress to evaluate the creep performance of materials. The temperature (T), stress (σ), and grain size (d) dependence of creep rate ($\dot{\epsilon}$) under steady-state condition is expressed using the following power-law relationship [65].

$$\dot{\epsilon} = A\left(\frac{b}{d}\right)^{p}\left(\frac{Gb}{kT}\right)D_0\left(\frac{\sigma}{G}\right)^{n} e^{\left(\frac{-Q_c}{RT}\right)} \qquad \text{Equation 6.1}$$

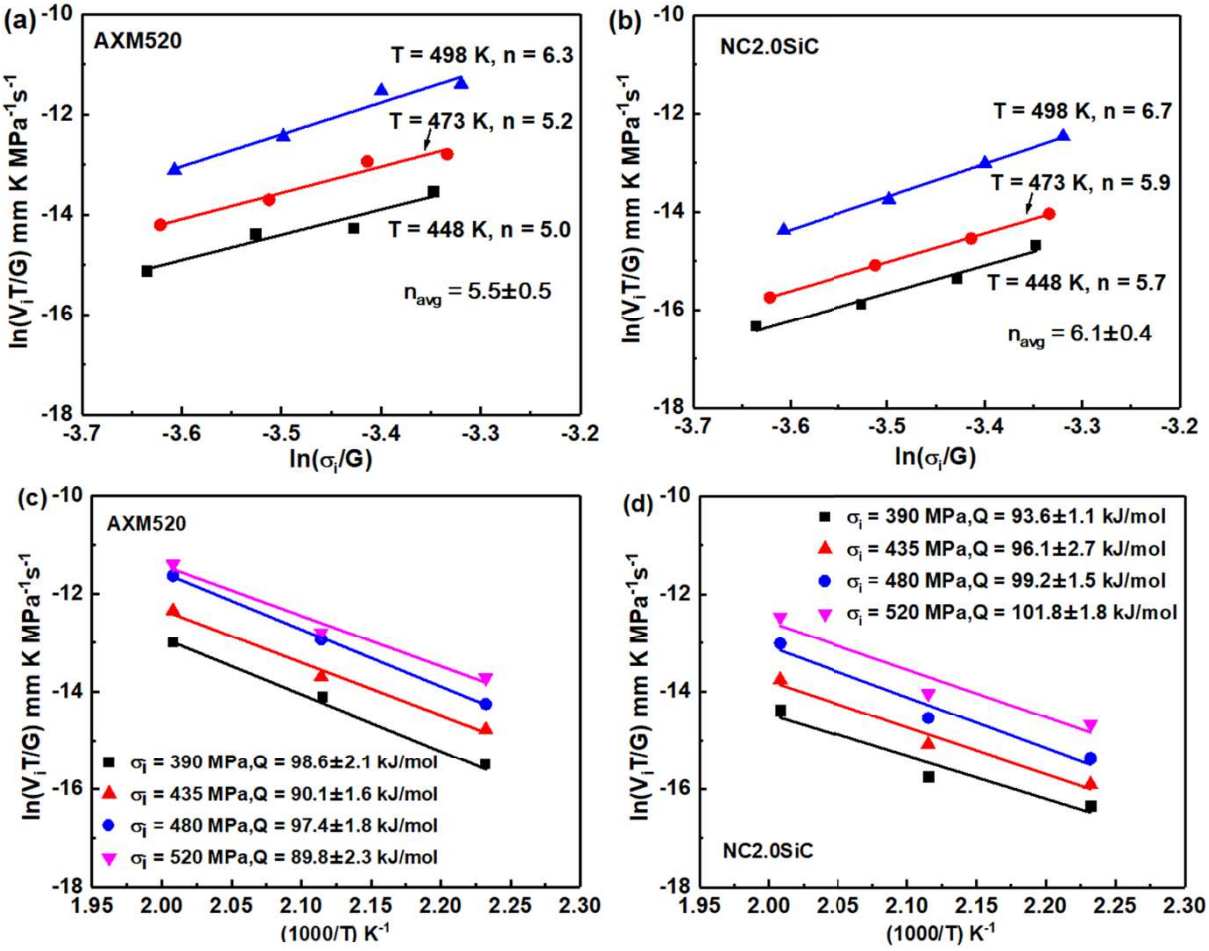

Figure 6.2 Stress dependence of the steady-state impression velocities at different temperatures for the (a) AXM520 alloy and (b) NC2.0SiC; temperature dependence of the steady-state impression velocities at different stresses for the (c) AXM520 alloy and (d) NC2.0SiC.

The σ and $\dot{\epsilon}$ in a tensile/compressive creep are related to the stress employed in impression creep (σ_{imp}) and impression velocity (V_{imp}) (calculated under steady-state) as follows:

$$\dot{\epsilon} = \frac{V_{imp}}{C_2 \emptyset} \text{ and } \sigma = \frac{\sigma_{imp}}{C_1} \text{ where } \sigma_{imp} = \frac{4F}{\pi \emptyset^2} \qquad \text{Equation 6.2}$$

Thus, the expression equivalent to equation (1) in an impression creep is given by [116].

$$\left(\frac{V_{imp}\, T}{G}\right) = B \left(\frac{\sigma_{imp}}{G}\right)^n e^{\left(-\frac{Qc}{RT}\right)} \qquad \text{Equation 6.3}$$

In equation 6.3, B is an overall pre-exponential constant. The definitions of the parameters of equations 6.1 to 6.3 are provided in Table 6.1. The value of shear modulus (G) decreases with an increase in temperature. Thus, an expression provided in [30] for Mg alloy is employed for temperature-compensated shear modulus. Stress exponents (n) and activation energies (Q) were evaluated from Equation 6.3 to ascertain the mechanism responsible for creep in the materials. A series of creep tests were conducted at varying stress and temperature. The n and Q values were evaluated from the gradients of $\ln\left(\frac{V_{imp}\, T}{G}\right)$ vs. $\ln\left(\frac{\sigma_{imp}}{G}\right)$ (at constant T), as well as $\ln\left(\frac{V_{imp}\, T}{G}\right)$ vs. $\left(\frac{1}{T}\right)$ (at constant σ) plots, respectively. The representative plots exhibiting the calculation of n and Q for AXM520 and NC2.0SiC are provided in Figure 6.2(a to d). The summary of n and Q values for all the materials employed are included in Tables 6.2 and 6.3, respectively.

Table 6.1 Definitions of the parameters used in the equations.

Symbols	Definition	Symbols	Definition
$\dot{\varepsilon}$	Steady-state creep rate (s^{-1})	**Q**	Creep activation energy (kJ. K^{-1}.mol^{-1})
A	A material constant	**R**	Universal gas constant (8.314 J. K^{-1}.mol^{-1})
b	Burgers vector (Å)	**T**	Absolute temperature (K)
D	Grain size (μm)	V_{imp}	Impression velocity (mm.s^{-1})
p	Inverse grain size exponent	**Ø**	Indenter (Punch diameter (mm))
G	Shear modulus (MPa)	**h**	Impression depth (mm)
D_0	Coefficient of self-diffusion	**F**	Applied load on punch (N)
K	Boltzmann's constant (1.38×10^{-23} kg.m^2. s^{-2}. K^{-1})	**B**	A constant
σ	Applied stress (MPa)	C_1, C_2	Constants
n	Stress exponent	σ_{imp}	Stress in impression creep (MPa)

Table 6.2 Summary of the n values obtained from the creep tests at different temperature levels.

Temperature (K)	Stress exponent (n)				
	AXM520	**NC0.5SiC**	**NC1.0SiC**	**NC2.0SiC**	**NC3.0SiC**
448	5.0	4.3	5.4	5.7	6.2
473	5.2	6.7	6.4	5.9	5.5
498	6.3	5.8	6.5	6.7	6.5
Average (n_{avg})	5.5±0.5	5.6±1.0	6.1±0.5	6.1±0.4	6.1±0.4

Table 6.3 Summary of the Q values obtained from the creep tests at different stress levels.

Stress (MPa)	Activation energy (Q) (kJ/mol)				
	AXM520	**NC0.5SiC**	**NC1.0SiC**	**NC2.0SiC**	**NC3.0SiC**
390	98.6±2.1	80.6±5.3	93.2±2.8	93.6±1.1	88.1±1.1
435	90.1±1.6	81.4±0.2	78.1±0.6	96.1±2.7	98.1±0.4
480	97.4±1.8	82.3±0.6	84.4±0.6	99.2±1.5	92.3±2.3
520	89.8±2.3	92.2±2.9	105.5±2.3	101.8±1.8	93.9±1.9

The n values for the alloy were 5.0 to 6.3, and the same for the nanocomposite was from 4.3 to 6.7, indicating that dislocation climb was the creep mechanism for all the materials. The Q values were in the range from 89.8±2.3 to 98.6±2.1 kJ/mol for the alloy, whereas the same was in the range from 78.1±0.6 to 105.5±2.3 kJ/mol for the NCs. The Q value in the present study lies between 78.1 to 105.5 kJ/mol. The energy needed for self-diffusion within the lattice of Mg is 135 kJ/mol, and the same for pipe-diffusion is 92 kJ/mol [117]. Therefore, the climb of dislocation assisted by pipe diffusion was the mechanism for creep deformation in the alloy and NCs at all the combinations of temperature and stress values utilized in the present study.

6.2 Post-creep microstructural analysis

6.2.1 Observation of sub-surfaces

The specimens of the AXM520 alloy and NC2.0SiC exposed to creep deformation at 435 MPa and 498 K were bisected along the diameter of the impressions to observe the microstructural changes below the indentation. One such bisected piece for each material was taken, and the surfaces below the indentation were observed under a microscope. Figure 6.3(a and b) exhibits the grain orientation map of AXM520 alloy and NC2.0SiC, respectively. The area mapped with identical color signifies the same orientation of the grains. The orientation maps of

AXM520 alloy and NC2.0SiC exhibited three separate regions below the indentation, namely R1, R2 and R3. The regions R1 and R3 correspond to undeformed zones below the indenter. The region R2 indicates the deformed region. The regions R1 and R3 exhibit comparatively larger grains than region R2. Additionally, region R2 displays a higher number of oriented grains than regions R1 and R3. The average widths of region R2 in the AXM520 alloy and NC2.0SiC was 203.8 ± 21.3 μm and 128.3 ± 15.2 μm, respectively. Thus, the extent of deformed zone of NC2.0SiC was less compared to the AXM520 alloy. The grain boundary maps taken from the AXM520 alloy and NC2.0SiC are shown in Figure 6.3(c and d). The grain that has miss orientation angle below 15 ° is known as a low-angle grain boundary (LAGB), while the high-angle grain boundary (HAGB) has a characteristic miss orientation angle greater than 15 °. The population of HAGBs is higher in the deformed region R2 compared to regions R1 and R3. The presence of a large population of HAGBs in R2 indicates that the grains in the plastically deformed region had undergone dynamic recrystallization owing to exposure at elevated temperature during the creep tests. Figure 6.3(e and f) exhibits the Kernel Average Misorientation (KAM) maps constructed from the deformed regions of both the AXM520 alloy and NC2.0SiC nanocomposite. The KAM map represents the average misorientation between a particular pixel and its specified nearest neighbor. The KAM maps estimate the deformation in crystals [118]. In the present investigation, for constructing the KAM maps the average misorientation of a particular pixel was calculated up to its three nearest neighbors with the provision that misorientation not exceeding 5 °. The different colours indicate the extent of local misorientation inside individual grain. Blue and red colours were for the grains without any misorientation (0 °) and the maximum misorientation (5 °), respectively. The changeover of the blue colour corresponding to the KAM distribution at low angle to yellow colour corresponding to higher angle indicates the increase in the grain boundary misorientation strain (GBMS) among the grains. Thus, the intensity of blue colour corresponding to region R2 is the highest compared to regions R1 and R3 in both the alloy and nanocomposite. The lower KAM value of the deformed region, R2, compared to the undeformed region, R3, was attributed to the dynamic recrystallization of the deformed region during the impression creep test. The creep tests were performed at a constant stress and constant temperature. The deformation and dynamic recrystallization took place simultaneously owing to the exposure to temperature for a long time. In addition, the intensity of blue colour in the region R2 of the nanocomposite reduced compared to that in the alloy indicating that the local GBMS was more in the nanocomposite.

The regions below indentations for AXM520 alloy and NC2.0SiC exposed to creep at 435 MPa and 498 K were further characterized using SEM, and the micrographs are shown in Figure 6.4(a and b). Three distinct regions below the indentation are observed, as discussed earlier. The deformation characteristics of the region below the cylindrical indenter in an impression creep is well explained using the typical Hertzian stress distribution employing [119]

$$\frac{\sigma_z}{p_m} = -\frac{1}{2}\left(1 - \frac{r^2}{a^2}\right)^{-1/2} \qquad \text{Equation 6.4}$$

where σ_z is the applied normal stress, P_m denotes the mean contact pressure below indentation, 'a' is the cylindrical flat indenter (punch) radius and r is the radial distance from the center of the indenter. At r = 0, i.e., at the center of the indenter, σ_z equals to -0.5P_m; and at r = a, i.e., at the edges of the indenter, reaches infinity at the edges of the indenter, i.e., r = a. Thus, the region immediately beneath the indenter, i.e., region R1, exhibits a low deformation region and forms a hemispherical dead zone. The region marked as R2 shows the characteristics of localized shear deformation owing to high stress concentration at the periphery of the indenter. The width of region R2 implies the ability of the material to withstand the applied stress. The extent of region R2 was different in AXM520 alloy and NC2.0SiC. Region R3, away from the indenter periphery, exhibits a microstructure comparable to the undeformed one, indicating that the stress experienced in this region was negligible.

The magnified view of region R2 in Figure 6.4(a) exhibits that the connectivity of the C36 phase in the AXM520 alloy was completely disintegrated and fragmented along the flow of the metal. The disintegration of the C36 phase was also observed in NC2.0SiC, as shown in Figure 6.4(b). However, the fragmentation of the C36 was not severe as compared to the AXM520 alloy. This indicates that additions of SiC_{np} in the AXM520 alloy improved deformation resistance of α-Mg. Thus, narrowing down the extent of region R2 in NC2.0SiC implies its improved creep response over AXM520 alloy. The improved strengthening of α-Mg matrix in NC2.0SiC was attributed to the Orowan strengthening imparted by the SiC nanoparticles. The presence of the C36 phase alone in AXM520 alloy provided the grain boundary pinning effect during creep deformation. However, the dispersion of SiC_{np} in AXM520 alloy strengthened the α-Mg matrix by Orowan strengthening. Thus, the creep performance of the NC2.0SiC was improved significantly than the AXM520 alloy. However, the effect of Orowan strengthening reduced when the fraction of SiC_{np} increases to 3.0 (wt.%) in NC3.0SiC. The declination in creep property of the NC3.0SiC was governed by the agglomeration of SiC_{np} as the amount of SiC increased.

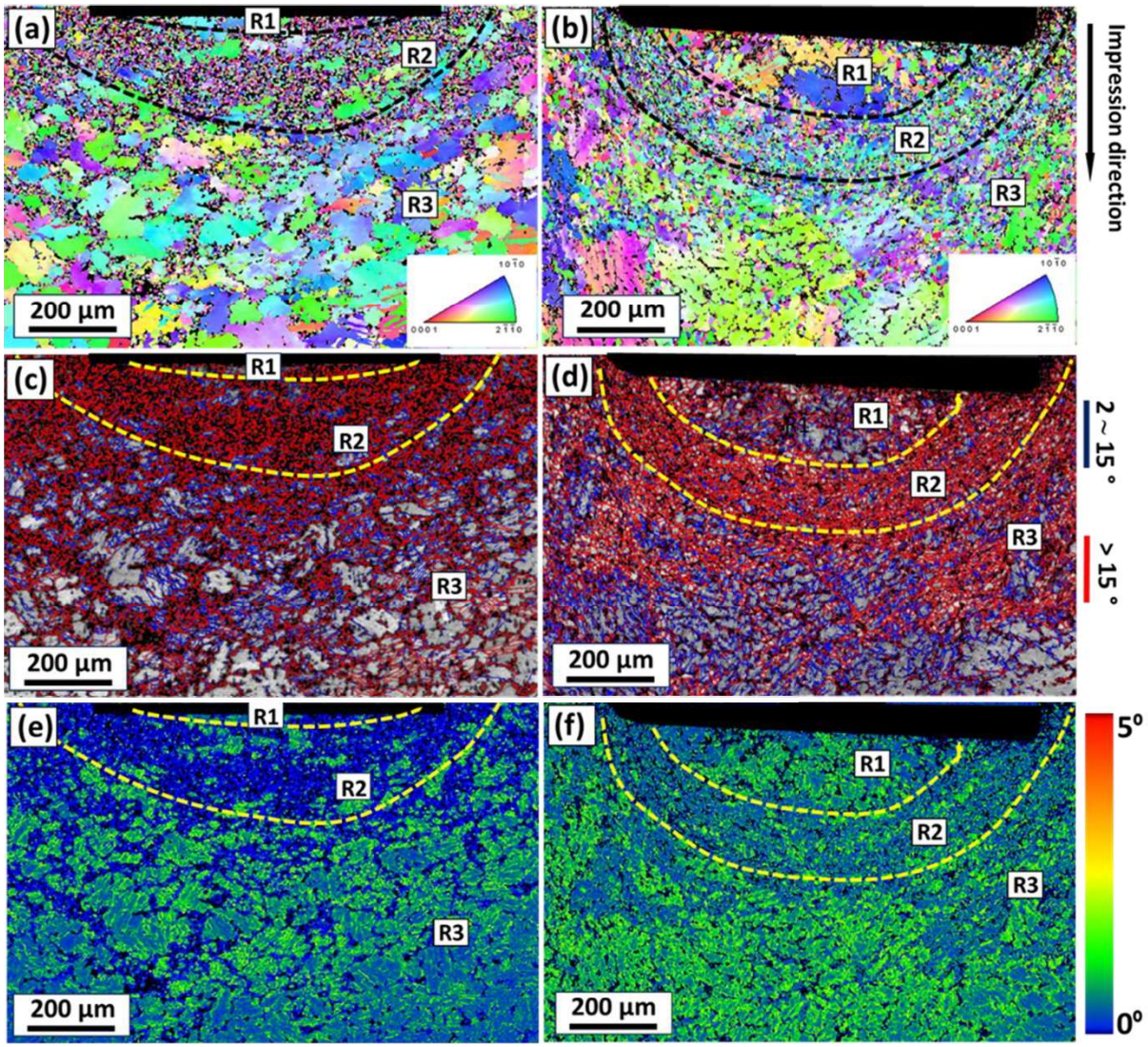

Figure 6.3 EBSD map of the creep tested samples showing grain orientation map under the punch for (a) AXM520 alloy, and (b) NC2.0SiC creep tested at 498 K and 435 MPa; corresponding grain boundary maps (c and d) and KAM maps (e and f) for the AXM520 alloy (from a) and NC2.0SiC (from b).

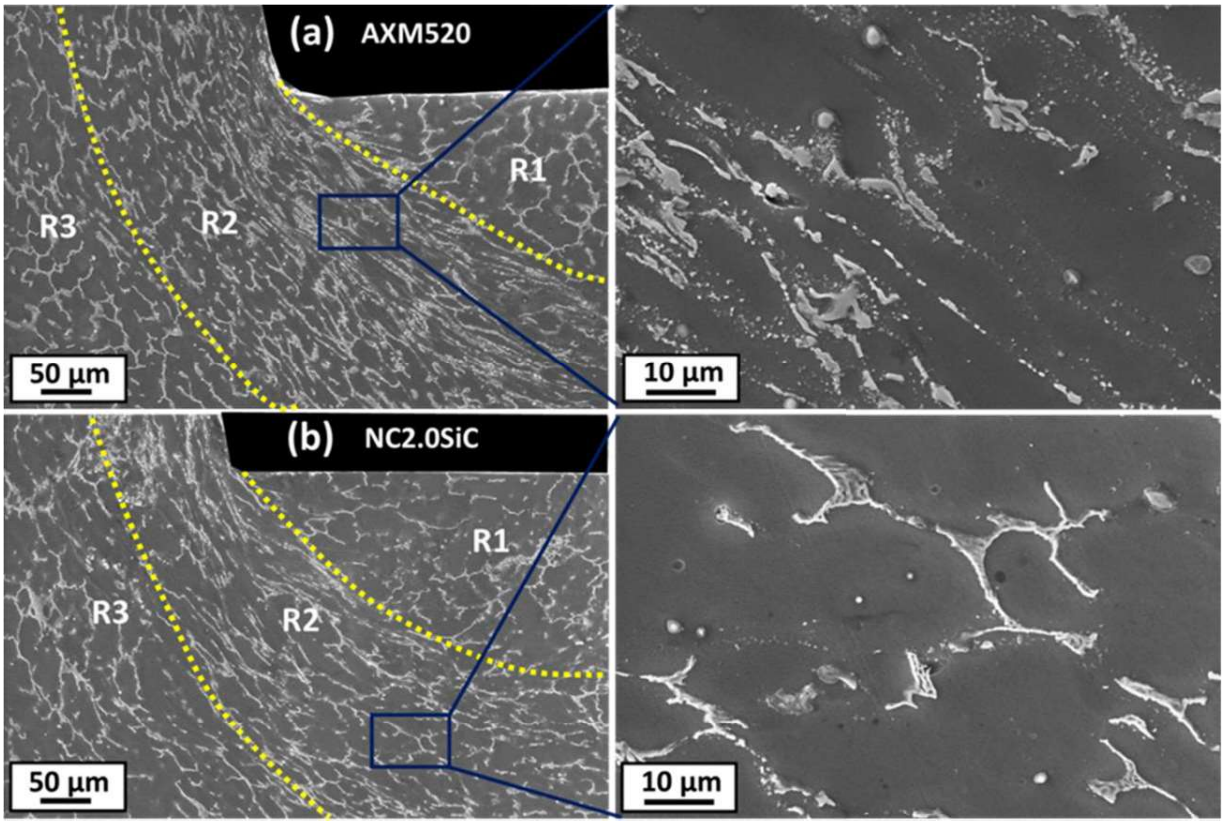

Figure 6.4 SEM micrographs displaying flow configuration underneath the indentations for the (a) AXM520 alloy, and (b) NC2.0SiC nanocomposite creep tested at 498 K and 435 MPa.

6.2.2 Observation of dislocations

The TEM brightfield (BF) images of the creep-exposed AXM520 alloy and NC2.0SiC specimens are shown in Figure 6.5(a to e). The presence of numerous dislocations is observed in the micrographs. Figure 6.5(a) exhibits the dislocation forest in the α-Mg matrix of the AXM520 alloy, and Figure 6.5(b) exhibits a planner defect bounded by two parallel edges. The presence of several dislocations within the planner defect is also noted. The characteristic of the planner defect in the micrograph is similar to that of twins. The formation of twins in the Mg alloys during creep deformation was described previously as well [120]. The dense dislocation network in the α-Mg matrix is portrayed in Figure 6.5(c). These features indicate that the dislocations interacted during movement, creating a dislocation network and dislocation entangled during creep deformation of the AXM520 alloy. The dislocations are free to move inside the grain during creep deformation under the applied stress in the absence of any obstacle. However, their movement is restricted once they reach the grain boundaries. This is because the regular arrangement of atoms at the grain boundary is broken, and there is a difference in orientation between the two grains. Thus, the grain boundaries act as an obstacle to the dislocation's movement. The dislocations created a pile-up around the C36 phase in the AXM520 alloy, as shown in Figure 6.5(d). The pile-up of dislocation provides a back stress to the incoming dislocations, which is one of the factors responsible for the work-hardening of the alloy. The presence of several dislocations within the grain is also observed. The presence of a secondary phase at the grain boundaries also impeded the motion of dislocations during the creep deformation. The SiC_{np} in the NC2.0SiC provided additional obstruction to the dislocation motion, and a pile-up of dislocation took place near the SiC nanoparticles, as shown in Figure 6.5(e). The SAED pattern acquired from Figure 6.5(e) is shown in Figure 6.5(f). The analysis of the SAED pattern confirms the presence of SiC_{np} in α-Mg. Thus, the additional strengthening owing to the presence of SiC_{np} in NC2.0SiC caused its superior creep performance over the AXM520 alloy. Figure 6.6(a to f) exhibits the BF and DF TEM micrographs taken with B = $[\bar{1}2\bar{1}1]$ from the grain interior (i.e., α-Mg phase) of the AXM520 alloy creep tested at 498 K and 435 MPa. The BF and DF images in Figure 6.6(a and b) reveal the dislocations in the selected region. To understand the nature of dislocations, the **g.b** analyses were performed. The <c> type dislocation inside the grain interior was made visible with **g**= {0002} and is presented in Figure 6.6(c and d). The <a> type dislocation in the same region was also made visible with **g**= $\{10\bar{1}0\}$ and is shown in Figure 6.6(e and f). The probable burger vectors of the dislocations are $\pm[11\bar{2}3]$, $\pm[\bar{2}113]$, $\pm[11\bar{2}\bar{3}]$, and $\pm[\ \bar{2}11\bar{3}]$ [121]. The presence

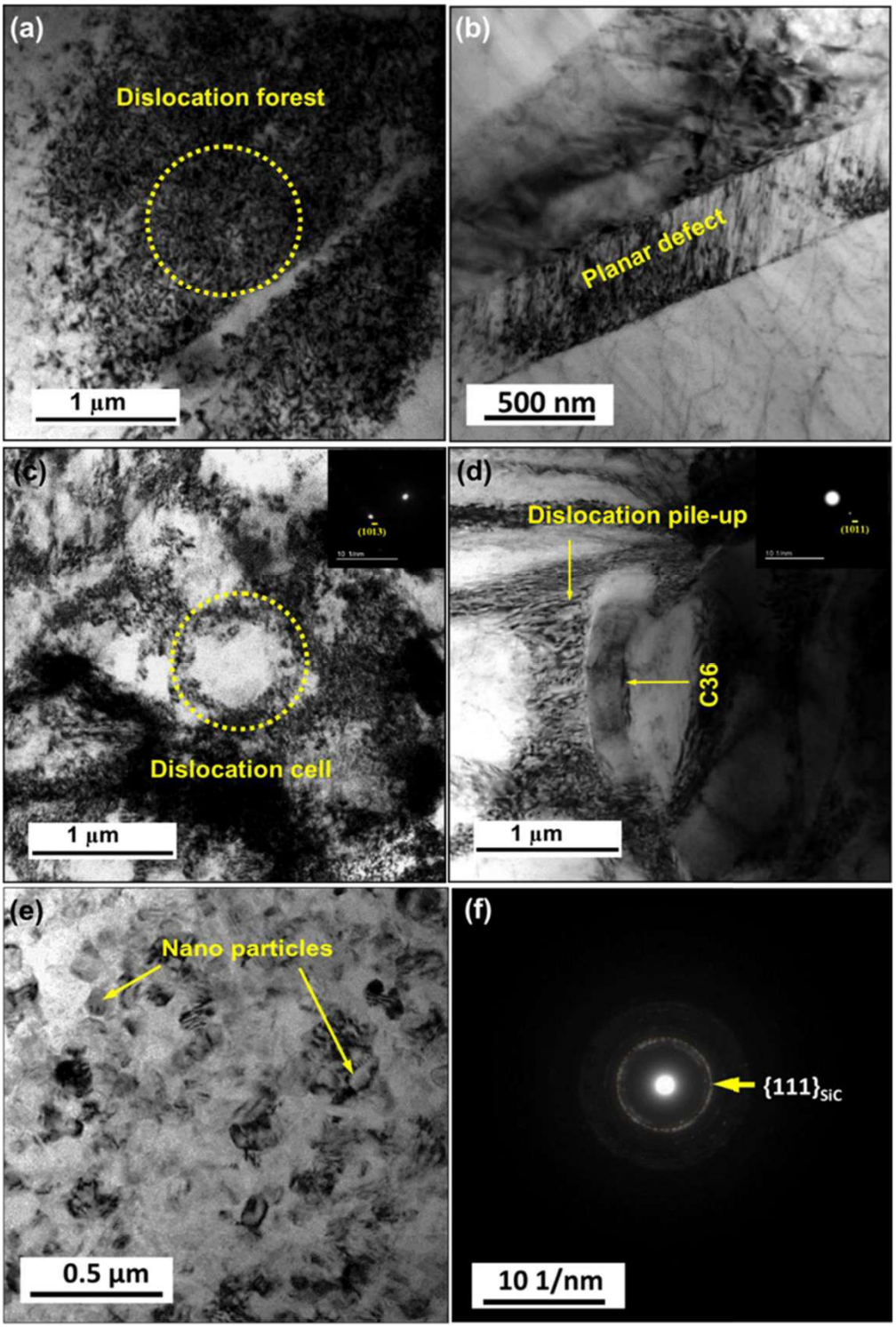

Figure 6.5 Bright Field (BF) TEM micrographs of the AXM520 alloy creep tested at 498 K and 435 MPa showing the (a) dislocation forest, (b) planner defect, (c) dislocation cell in the α-Mg matrix, and (d) dislocation pile-ups around the C36 phase; (e) BF TEM micrograph micrographs of the NC2.0SiC nanocomposite creep tested at 498 K and 435 MPa showing the dislocation pile-ups near the nanoparticles, and (f) SAED pattern taken from 'e'.

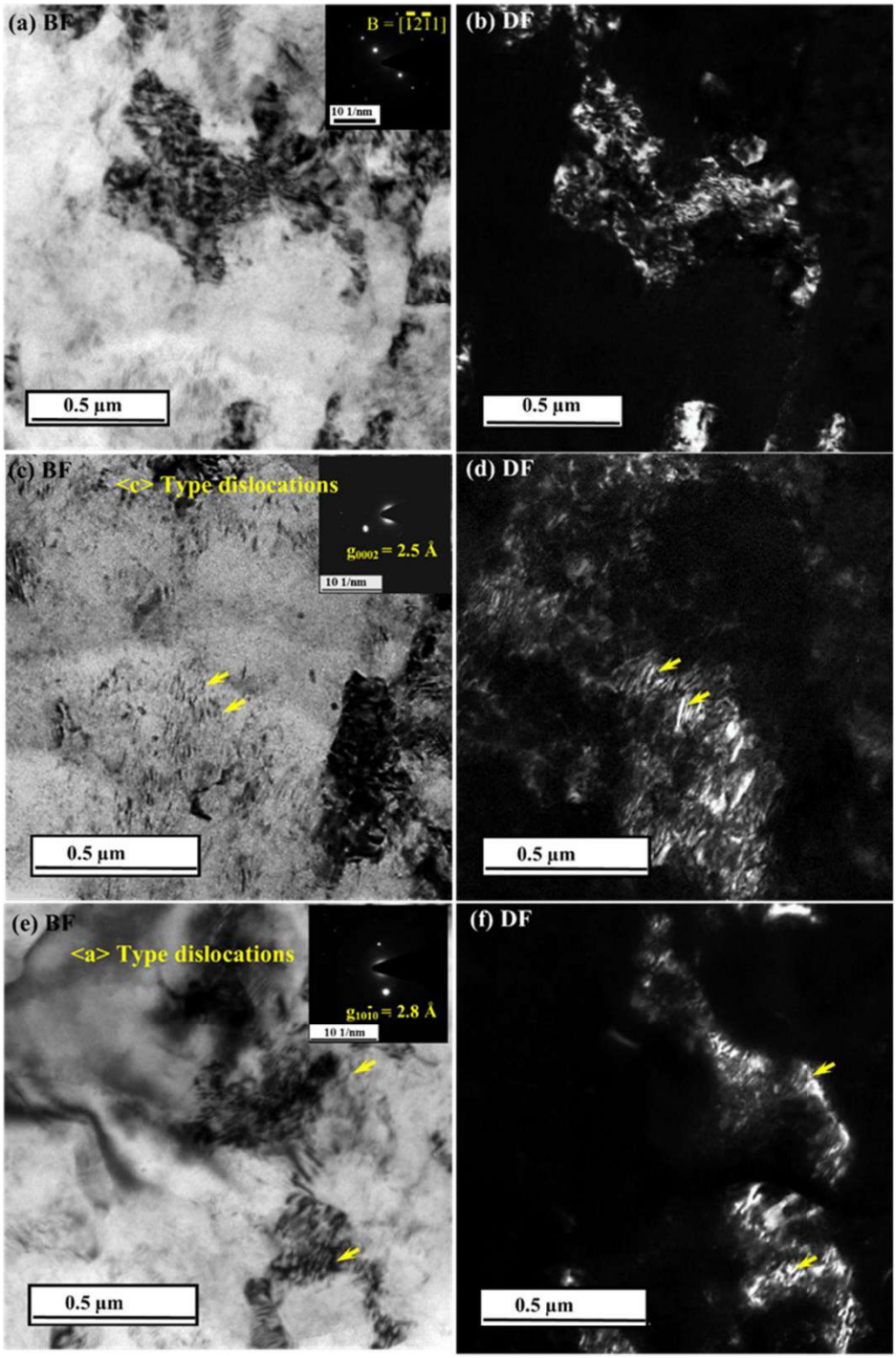

Figure 6.6 BF (a) and DF (b) TEM micrographs taken with B = [1$\bar{2}$1$\bar{1}$] from the grain interior (i.e., α-Mg phase) of the AXM520 alloy creep tested at 498 K and 435 MPa depicting the dislocations; BF (c) and DF (d) TEM micrographs taken with $\overrightarrow{g_{[0002]}}$ reveal the presence of <c> type dislocation in 'a'; BF (e) and DF (f) TEM micrographs taken with $\overrightarrow{g_{[10\bar{1}0]}}$ reveal the presence of <a> type dislocation in 'a'.

of the <c> type dislocation indicates the activation of the <c> slip plane at elevated temperature. In addition, the dissociation of the <c+a> dislocation into <a> and <c> components and the subsequent annihilation of the <a> dislocation (basal component) by glide leave the <c> dislocation [122,123].

6.3 Summary of chapter 6

In this chapter, the detailed creep behavior of the squeeze-cast Mg-5.0Al-2.0Ca-0.3Mn (wt.%) (AXM520) alloy and NCs has been presented. The major findings from the current chapter are summarized below.

i. The NCs revealed improved creep performance compared to the AXM520 alloy under the experimental parameters utilized. The creep resistance of the NCs increases with the increase in the SiC_{np} content. The NC2.0SiC exhibited an increase in creep resistance by 73.2% compared to the alloy. However, the creep resistance deteriorated with a further increase in the fraction of the SiC_{np} in the NC3.0SiC, due to the agglomeration.

ii. The stress exponents varied from 5.0 to 6.7, and activation energies varied from 89.8 to 101.8 kJ/mol, implying the deformation at elevated temperature in the AXM520 alloy and NCs was dominated by the climb of dislocation assisted by the pipe diffusion.

iii. The pile-ups of dislocations took place around the C36 phase and near the SiC_{np}. The additional strengthening owing to the presence of the SiC_{np} in the NCs was responsible for their improved creep performance compared to the AXM520 alloy.